A Hexagonal Pseudo-Polar FFT for Formation-Flying Interferometric Radiometry

Ahmed Kiyoshi Sugihara El Maghraby, Angelo Grubišić, Camilla Colombo and Adrian Tatnall

***Abstract*—A novel mission concept applying satellite formation flight to passive microwave interferometry was recently proposed to significantly improve the interferometer's spatial resolution. This concept was shown to sample the visibility in a hexagonal tile of polar grids, and to recover the brightness map, this visibility must be inverted via a discrete polar inverse Fourier transform. For a fast and accurate solution, this letter develops a modified hexagonal variant of the Pseudo-Polar Fast Fourier Transform (PPFFT) and its inverse, and explores its performance when applied to the proposed formation-flight radiometer. Compared to the conventional rectangular PPFFT, we find approximately a five-fold improvement in the recovered radiometric accuracy, where the RMS radiometric error is in the order of 10^{-2} K. The impact of visibility interpolation method is also explored, showing that an FFT-based interpolation technique leads to the most accurate final image recovery.**

***Index Terms*—Synthetic aperture imaging, image reconstruction, microwave radiometry, satellite formation flight, mission concept.**

I. Introduction

MICROWAVE radiometers are highly versatile Earth observation instruments which map the brightness temperature of the Earth at specific microwave frequency bands. Careful choice of the frequency allows the observation of different features of the Earth; for example the L-band (1.4 GHz) is most sensitive to ocean salinity and soil moisture, and radiometry at the resonance frequencies of oxygen and water molecules is the basis of atmospheric sounding. While real-aperture radiometers rely on scanning reflectors to map the brightness temperature, interferometric — i.e., synthetic aperture — radiometers produce the map using a set of coherent receivers, ridding the need for large scanning mechanisms thus enabling the synthesis of very large apertures, as demonstrated by the Soil Moisture and Ocean Salinity mission (SMOS) [1].

Recent years have seen a remarkable acceleration in the development of geostationary interferometric radiometer systems for atmospheric sounding. The development of the rotating interferometers, e.g., the Geostationary Atmospheric Sounder (GAS) [2] and the Geostationary Interferometric Microwave Sounder (GIMS) [3] has brought in demand a fast and accurate method for polar Fourier transform for image reconstruction. The problem stems from the fact that interferometric radiometers do not measure the brightness temperature directly, but instead they measure an intermediary quantity known as the visibility function, which is related to the brightness temperature via the Van Cittert-Zernike theorem, stating that the visibility function is the spatial Fourier transform of the modified brightness temperature map, as follows. [4], [5]

Manuscript received February 07, 2018; revised June 29, 2018; accepted August 04, 2018. Date of publication January XX, XXXX. This work has been funded by the UK Engineering and Physical Sciences Research Council (EPSRC). Award Reference number 1503202.

Ahmed Kiyoshi Sugihara El Maghraby and Angelo Grubišić are with the Astronautics Research Group at the University of Southampton, Southampton, United Kingdom (e-mail: asem1g14@soton.ac.uk, a.grubisic@soton.ac.uk). Camilla Colombo is with the Department of Aerospace Science and Technology, Politecnico di Milano, Milan, Italy (e-mail: camilla.colombo@polimi.it). Adrian Tatnall was with the Astronautics Research Group at the University of Southampton, Southampton, United Kingdom (e-mail: art4@soton.ac.uk)

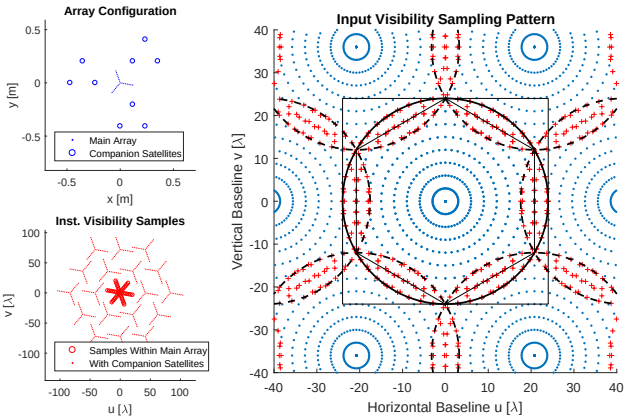

(a) (b)

Fig. 1. Nine-cubesat configuration for the proposed interferometer (a, top) and its instantaneous sampling pattern (a, bottom). Rotation of the central array leads to a hexagonal tile of polar grids (b). + shows the overlapping regions. The hexagon shows the area in which the proposed hexagonal PPFFT grids are interpolated, while the square shows that for the conventional PPFFT.

$$\hat{T}_B(\xi,\eta) = \iint_{-\infty}^{+\infty} W(u,v)\cdot V(u,v)\cdot e^{2\pi i(u\xi+v\eta)}\mathrm{d}u\mathrm{d}v \quad (1)$$

Here $\hat{T}_B(\xi,\eta)$ is the recovered modified brightness temperature map of the target, where $[\xi,\eta]$ are the direction cosines. $V(u,v)$ is the visibility function, where $[u,v]$ are the horizontal and vertical components of the baseline vector, and $W(u,v)$ [6] is a window function designed to reduce Gibbs ringing.

In practice, interferometers measure the visibility function as a set of point-samples. Given a pair of antennas separated by a known distance $[u,v]$, called the baseline vector, the microwave signals each of these antennas receive from the source, i.e., Earth, are cross-correlated to produce a single Hermitian pair of visibility samples at points $[u,v]$ and $[-u,-v]$. The set of all possible baseline pairs produce the visibility sample set. Polar sampling grids arise from rotating interferometers, e.g., GAS and GIMS. The rotating design is

motivated by the need to minimise system complexity and mass, where the rotation allows each antenna pair to take multiple visibility samples as they move in space, minimising the required number of antennas. From these samples, the brightness temperature map of the Earth is recovered via discrete inverse Fourier transform. Here it must be highlighted that the method that best suits the application depends closely on the given type of grid. For example, the SMOS mission produces a hexagonal grid, therefore the hexagonal FFT is the fastest and most accurate method [7], while for GIMS the pseudo-polar FFT (PPFFT) has shown the best results [8].

Now, a multi-satellite interferometric radiometer concept has been described in [9] which uses inter-satellite baselines to achieve unprecedented baseline lengths, thus significantly improving the interferometers spatial resolution. Fig. 1a shows the formation configuration for a 9-cubesatellite design, and the resultant visibility sampling pattern is shown in Fig. 1b. The grid is a hexagonal tile of overlapping polar grids. As the central satellite rotates, the central part of Fig. 1b is sampled by central satellite on its own, while baselines between different satellites — i.e., the inter-satellite baselines — produce the remaining samples, highlighted in dashed contours.

While the conventional rectangular PPFFT can still be applied to invert this set of visibility samples, it is found that the overlapping areas introduce a strong noise at the polar grids' interfaces with neighbouring grids (see Fig. 6a right). If a grid can be found that can be tiled without overlaps, we can expect a significant improvement in the accuracy of the recovered map. In this pursuit, we develop a new hexagonal variant of the PPFFT method.

II. The Hexagonal Pseudo-Polar Fast Fourier Transform

The conventional PPFFT applies the combination of 1-D FFT and 1-D fractional Fourier transform — for which fast algorithms are available — to find the Fourier transform of an input image in the pseudo-polar grid. Averbuch et al. [10] have presented a comprehensive description of the rectangular PPFFT and its inverse, and Zhang et al. [8] have presented the technique as an effective method to invert the visibility sampled by the rotating radiometer GIMS. The method in [11] further generalises the PPFFT to include polygons of multiples of four, however the hexagonal case still remains unexplored. Based on these precedents, the following paragraphs describe the forward and inverse transforms to the hexagonal grid.

Given an N by N input image, hexagonal PPFFT outputs three N by 2N grids designated as G_1, G_2 and G_3, the arrangement of which is shown in Fig. 2. The axes ξ_ξ and ξ_η are as defined in [10], where they refer respectively to the horizontal and vertical components of the angular spatial frequency present in the discrete N by N image. The conventional two-dimensional FFT produces an equispaced N by N rectangular grid within the 2π by 2π square, which is also the area the rectangular PPFFT covers. Unlike the rectangular PPFFT, the hexagonal grid does not capture all spatial frequency content present in the input image. This is to allow all spatial frequency samples in the hexagonal grid

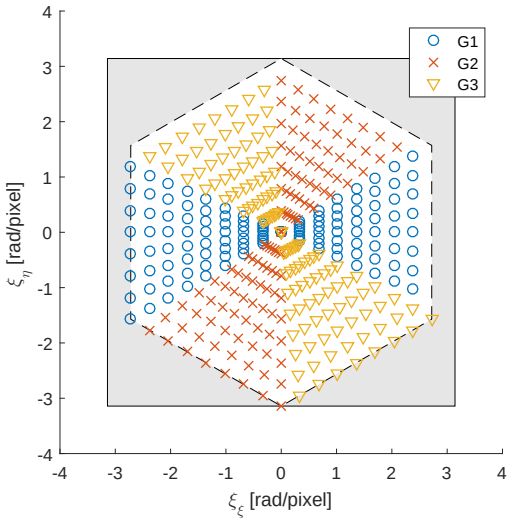

Fig. 2. Proposed hexagonal PPFFT grid with N=8. Shaded area shows the full spatial frequency content of the input N by N image, and the hexagon shows the tile size.

to remain within the frequencies reproducible by the original N by N image. This means the forward hexagonal PPFFT is a lossy process if the input image contained frequencies outside the hexagonal area, shown by the shaded square in Fig. 2. This is acceptable for our application however, since we are concerned with the inverse PPFFT, in which we start with the hexagonal grid, for which we can losslessly recover their spatial frequency components. To achieve this, the hexagonal PPFFT requires two 1-D Fractional FFTs. The hexagonal PPFFT process to find G_1 is defined as follows.

1) The input N by N image, g_1, is zero-padded to N by 2N, with indexes $0 \leq k_1 < N$ and $0 \leq k_2 < 2N$. A single-dimensional fractional Fourier transform is taken in the horizontal direction as follows.
$$\tilde{g}_1[k_1, l] = \sum_{k2=0}^{2N-1} g_1[k_1, k_2] \cdot exp\left(\frac{-2\pi i k_2 l}{2N}\frac{\sqrt{3}}{2}\right) \quad (2)$$
with index $-N \leq l < N$. The fractional Fourier transform can be evaluated using three FFTs [12].
2) Fractional Fourier transform is then applied to each column with the fraction α gradually shifting from $-\frac{\sqrt{3}}{2}\frac{1}{\sqrt{3}} = -\frac{1}{2}$ to $\frac{1}{2}$, defined as follows.
$$G_1[m, l] = \sum_{k1=0}^{N-1} \tilde{g}_1[k_1, l] \cdot exp\left(\frac{-2\pi i k_1 m}{N}\frac{l}{2N}\right) \quad (3)$$
with $-\frac{N}{2} \leq m < \frac{N}{2}$.

As inherent to FFT, this method presumes the cell $k_1 = k_2 = 0$ as the origin of the input image. To shift this origin to $k_1 = k_2 = \frac{N}{2}$, the following may be applied.
$$G_1^*[m, l] = G_1[m, l] \cdot exp\left[\frac{\pi i}{2}\left(m\frac{l}{N} + l\frac{\sqrt{3}}{2}\right)\right] \quad (4)$$

To find the G_2 and G_3 sets, the input image is rotated about $k_1 = k_2 = \frac{N}{2}$ by 60 and 120 degrees clockwise respectively, and the above process is repeated.

While the process is strictly speaking irreversible due to incomplete rank [10], an iterative approach as described by Averbuch et al. shows a reliable inverse PPFFT process. For this the adjoint transfer process is defined.

$$\hat{g}_1[k_1,k_2] = \sum_{m=-\frac{N}{2}}^{\frac{N}{2}-1}\sum_{l=-N}^{N-1} G_1[m,l]\cdot\frac{\sqrt{3}}{2}\cdot|\frac{l}{2N}|\cdot\frac{1}{2N^2} \cdot exp\left(\frac{2\pi i k_1 m}{N}\frac{l}{2N}+\frac{2\pi i k_2 l}{2N}\frac{\sqrt{3}}{2}\right) \tag{5}$$

which is followed by the image recombination process

$$\hat{g}_k = \hat{g}_{1k} + \mathrm{rot60}(\hat{g}_{2k}) + \mathrm{rot120}(\hat{g}_{3k}) \tag{6}$$

where rot60 and rot120 are the 60- and 120-degree anti-clockwise rotation processes respectively, about $k_1 = k_2 = \frac{N}{2}$. The scalar weights $\frac{\sqrt{3}}{2}$, $|\frac{l}{2N}|$ and $\frac{1}{2N^2}$ account for the differential area corresponding to, respectively, the horizontal and vertical fractional Fourier transforms and the discrete N by 2N Fourier transform. The iteration procedure is then as follows.

$$g_{k+1} = g_k - T_{PP}^H(T_{PP}(g_k) - G) \tag{7}$$

Where G is the concatenation of G_1, G_2 and G_3, g_k is the N by N iteration image initialised as a zero matrix, $T_{PP}()$ is the forward PPFFT process finding the three grids concatenated to a single matrix G_k, and $T_{PP}^H()$ is its adjoint process. G_k converges from a zero matrix to the given G. Here, $T_{PP}^H(T_{PP}(g_k)-G)$ is the residual, and the stopping condition is when the RMS of this map falls under a specified threshold.

One key consideration here is that the 60- and 120-degree rotations of the input image when finding grids G_2 and G_3 mean that G_2 is not sensitive to sources in areas 2 and 4 in Fig. 3b, and neither is G_3 to areas 3 and 4. Equivalently, the rotations of g_2 and g_3 made as part of the recombination process cause the edges of these grids to fall out of g_1, which is the output grid. Both of these properties mean that the hexagonal PPFFT is unable to reconstruct objects lying in areas 2, 3 and 4, and these areas are set to zero at the end of every iteration to ensure convergence. This is acceptable in the presented application, however, when the image contains objects in these areas, it must be zero-padded to ensure the areas 2, 3 and 4 are zero before forward transformation.

Further, it is found that the rotation process is a key step that can introduce significant noise when performed poorly. Unlike the 90-degree rotation required for the conventional PPFFT, for which an exact solution is available, the 60- and 120-degree rotations require two-dimensional image interpolation. Several interpolation methods are tried as presented in Table I, finding that the FFT interpolation produces the best result. This method [13] first applies a two-dimensional FFT to the input array, zero-padding the result in the frequency domain and applying an inverse FFT to recover the interpolated image.

The processes so far recover an image from a pseudo-polar grid of visibility. The remaining task is to interpolate the visibility from the polar grid to the pseudo-polar grid, which can be done in two steps of single-dimensional interpolation: first interpolating in the angular direction, followed by the radial direction. For the first step it has been found that the cyclic

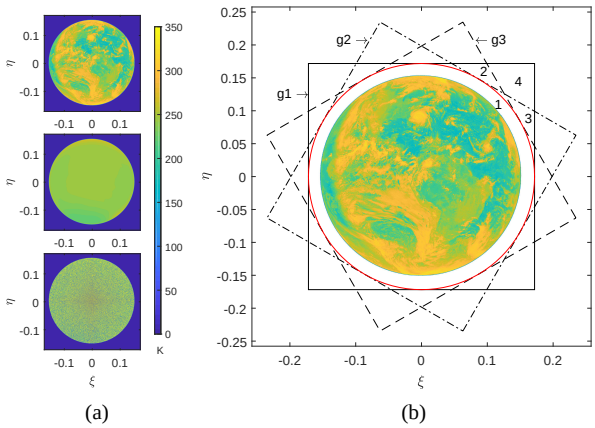

Fig. 3. Tested input brightness temperature maps (a). Input image shown in scale, as viewed from the geostationary orbit (b). Subgrids G_1, G_2 and G_3 recover sub-images g_1, g_2 and g_3 respectively. The 60- and 120-degree rotations mean that only area 1 contains contributions from all sub-images.

sinc interpolation is suitable [8]. Radial interpolation drives the quality of the recovered image, as this is the dimension with sparse sampling (see Fig. 1b). In Table I we compare linear, spline and FFT interpolation, and again we find the FFT method most suitable. Note that if we wish to recover the brightness temperature map centred at $k_1 = k_2 = \frac{N}{2}$, the interpolation process maps to G^* in (4), and not G.

III. Simulation Results

Now we evaluate the performance of the proposed method at reconstructing the brightness temperature map from a visibility set taken by the proposed multi-satellite interferometer. We simulate the full-size array, with nine cubesatellites and 236 elements per arm. This generates 19 polar grids, seven of which are as shown in Fig. 1b. One of these grids is considered at a time and interpolated into the PPFFT grid. The proposed hexagonal grid corresponds to the hexagonal area shown in Fig. 1b, while the conventional PPFFT corresponds to the square. The sum of the recovered maps from all 19 grids produces the final map. The Blackman window [6] is applied to the visibility samples prior to inverting, and the radiometric error map is defined as the difference between the recovered map and the original map passed through the Blackman low-pass filter to account for the radiometer's spatial resolution. The RMS is taken within the central part of this map (see Fig. 5), and reported in Fig. 4 and Table I.

To compare the proposed method against the method proposed in [9], the same input image of the Earth is used, as shown in Fig. 3a (top), and the visibility samples are obtained in the same manner, summarised as follows. The input 2048 by 2048 image is zero-padded by a factor of 8 and its FFT is taken, producing an over-sampled visibility given in a Cartesian grid. Our input visibility samples are interpolated from within this grid to the grid pattern shown in Fig. 1b, via two-dimensional planar spline interpolation. To ensure that the error introduced by this method is sufficiently low, we use the Shepp-Logan phantom [14], amplified in magnitude by a factor of 200 to better represent the brightness temperature of the Earth, to compare the brightness temperature error for the case

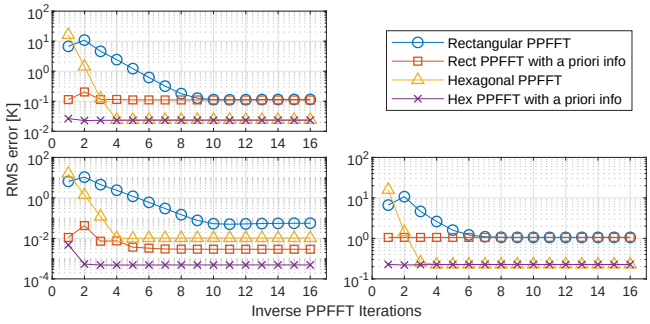

Fig. 4. The radiometric accuracy of g_k at successive iterations of the iterative inverse PPFFT for input images 1 (TL), 2 (BL) and 3 (BR), measured as an RMS error within the area shown in Fig. 6. The rectangular and hexagonal pseudo-polar grids are run with and without pre-processing with a priori information. Note this is not a measure of the residual of the iteration process.

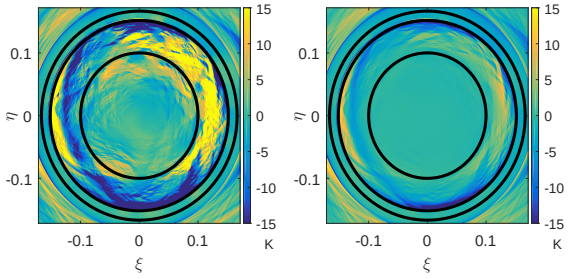

Fig. 5. Error map of input 1 recovered with linear visibility interpolation (left) and spline interpolation (right). Both cases exhibit sensitivity loss away from the origin. RMS is taken within the inner ring. Middle ring is the Earth-sky horizon, and the outer is the interferometer's Alias-Free Field of View.

the visibility is taken analytically, against the case the visibility is taken by interpolation. The disagreement between the two cases was 7.0×10^{-4} K. Two other input images are tested to study the method's response to extreme scenarios. Shown in Fig. 3a (mid) is a simulated map at 53 GHz, produced by the SAIRPS simulator [15]. Since the map is extremely smooth, we expect to see the best performance from this map. Then, we add a Gaussian white noise to this image with 1σ = 100 K to represent the opposite extreme, as shown in Fig. 3a (bottom).

Fig. 4 shows the convergence rate of the retrieval method shown in (7). Both the raw visibility and the pre-processed visibility using a-priori information, as suggested in [16], are inverted. This information includes the locations of the Earth-sky horizon, the sun and the moon, and the average brightness temperatures of the Earth, sun, moon and the background radiation. Pre-processing the visibility measurements results in an almost immediate convergence.

Table I shows the impact of visibility interpolation technique in the radial direction to the radiometric accuracy of the reconstruction method, for the raw and pre-processed sets of visibility samples. The cyclic sinc interpolation is used for the angular direction for all cases. The poor performance of linear and spline interpolations were expected since the 3λ sampling period of the interferometer is just under the Nyquist limit, which is 3.29λ [9]. Fig. 5 shows the brightness temperature error maps for linear (left) and spline (right) interpolation, for the pre-processed visibility samples. Severe

TABLE I
RADIOMETRIC ERROR OF RECOVERED MAP BY VISIBILITY INTERPOLATION AND IMAGE ROTATION TECHNIQUES

Interpolation Technique		Visibility Interpolation (Radial)				Image Rotation [K]	
		Rectangular PPFFT [K]		Hexagonal PPFFT [K]			
		raw	apr.	raw	apr.	raw	apr.
Im. 1	Lin.	35.8	3.49	35.8	3.50	3.86	2.33
	Spl.	7.82	0.54	8.00	0.43	0.77	0.70
	FFT	0.11	0.11	0.02[a]	0.02[b]	0.02[a]	0.02[b]
Im. 2	Lin.	34.91	0.65	34.94	0.61	0.07	2.9E-3
	Spl.	7.28	0.20	7.57	0.23	0.02	1.0E-3
	FFT	0.06	2.9E-3	0.01[c]	4.9E-4[d]	0.01[c]	4.9E-4[d]
Im. 3	Lin.	35.79	7.64	35.82	7.59	36.53	19.98
	Spl.	7.38	1.21	7.61	0.63	7.92	7.15
	FFT	1.06	1.05	0.23[e]	0.23[f]	0.23[e]	0.23[f]

All results after 16 iterations, for linear, spline and FFT interpolation. All image rotation techniques apply FFT visibility interpolation. Im. 1 through 3 = input images shown in Fig. 3a top to bottom. a pr. = a priori information applied prior to inversion. Pairs [a] through [f] are the same values.

loss of sensitivity is seen away from the origin as both methods struggle to interpolate the high frequency sinusoids in the visibility domain, which are responsible for off-axis sources. The interferometer's Alias-Free Field of View is marked by the outer-most circle, beyond which the first alias of the Earth is visible. Table I also lists the performance of the three interpolation methods for image rotation processes, and again the FFT method produces the best radiometric accuracy.

In practice, a threshold residual will be set as a stopping condition for the iteration process. Fig. 6 shows the results for input 1 with 1×10^{-3} K threshold. The conventional method converges in 11 iterations while the hexagonal method converges in 4 iterations. Fig. 6a (left) is the radiometric error map for the conventional PPFFT, and (right) is the Fourier transform of this map, produced by simply applying an FFT to the left image. This map clearly shows the spikes present at the boundaries of the overlapping polar grids. This noise can be attributed to the fact that the overlapping visibility samples are selected discretely, as shown in Fig. 1b as +, and this discrete choice can cause strong quantisation error if sampling is sparse. The hexagonal PPFFT reduces this noise by eliminating these overlaps. In Fig. 6b (right) the interfaces between neighbouring grids are much smoother, with the circular spikes removed. The noise levels within the hexagonal grids are in fact slightly higher compared to the conventional PPFFT due to the image rotation processes. However, the total noise level shows a factor of 4.8 improvement for this particular input with 0.023 K error, shown in Fig. 6b. The best and worst cases tested with inputs 2 and 3 indicate improvement factors of 6.0 and 4.7 respectively.

Finally, we note that the proposed method does not attempt to remove aliases. Strong alias of the sun, in particular, can substantially reduce the radiometric accuracy in the aliasing regions, thereby limiting the advantage of the method to the conventional PPFFT. Fig. 7 shows the worst cases for the two methods when the sun appears just next to the Earth. We can see both methods are convergent, and suffer equally from the alias. Aliases of the moon and other celestial bodies are negligible compared to the Earth's brightness temperature.

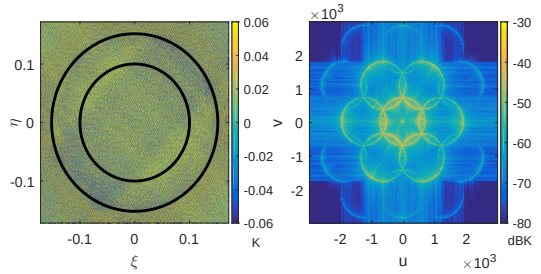

(a) Conventional PPFFT, RMS = 0.111 K

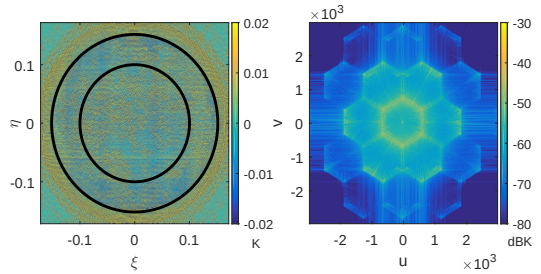

(b) Hexagonal PPFFT, RMS = 0.023 K

Fig. 6. Recovered brightness temperature error maps for the conventional and the proposed method, applied on input 1 with 10^{-3} K threshold residual. Spatial distribution of the error (left) and spatial frequency distribution (right).

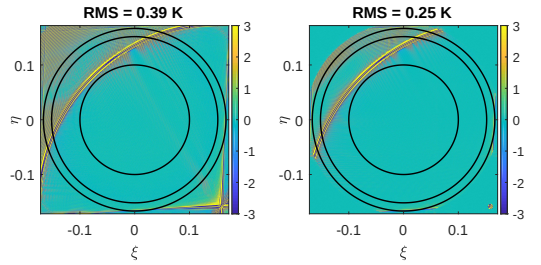

Fig. 7. Radiometric error map for input 2 when the sun's first alias enters the image, for conventional PPFFT (left) and the proposed method (right).

IV. Conclusion

A novel hexagonal variant of the Pseudo-Polar FFT and its inverse have been developed to recover the Earth's brightness temperature map from the visibility sampled by the proposed multi-satellite interferometric radiometer. Compared to the conventional rectangular PPFFT, the proposed method achieves approximately a five-fold improvement in the recovered radiometric accuracy when applied to the proposed interferometer. Three input maps have been tried, representing the brightness temperature map of the Earth at various frequencies. The best result is achieved for the smoothest map (Im 2) with a factor of 5.95 improvement, while the roughest map (Im 3) showed 4.67, and the average expected map (Im 1) showed 4.73. The proposed method requires that the corners of the rectangular input image are empty. When objects exist in these corners, e.g., the sun, the method converges with these objects removed. To fully harness the advantages of this method, a separate method is needed to remove the aliases of the sun, by either subtracting the brightness temperature map of the sun from the visibility samples prior to image recovery, or by post-recovery deconvolution, e.g., CLEAN.

Acknowledgments

The authors would like to thank Prof. Adriano Camps and Dr. Hyuk Park of the RSLab, Polytechnic University of Catalonia for generating the 53 GHz input image using SAIRPS. Further, the authors would like to thank the anonymous reviewers for their thorough and constructive comments.

All data supporting this study are openly available from the University of Southampton repository at https://doi.org/10.5258/SOTON/D0682.

References

[1] J. Font, A. Camps, A. Borges, M. Martin-Neira, J. Boutin, N. Reul, Y. H. Kerr, A. Hahne, and S. Mecklenburg, "Smos: The challenging sea surface salinity measurement from space," *Proc. of the IEEE*, vol. 98, no. 5, pp. 649–665, May 2010.

[2] A. Carlstrom, J. Christensen, J. Embretsen, A. Emrich, and P. de Maagt, "A geostationary atmospheric sounder for now-casting and short-range weather forecasting," in *2009 IEEE Antennas and Propagation Society International Symposium*, June 2009, pp. 1–4.

[3] C. Zhang, H. Liu, J. Wu, S. Zhang, J. Yan, L. Niu, W. Sun, and H. Li, "Imaging analysis and first results of the geostationary interferometric microwave sounder demonstrator," *IEEE Transactions on Geoscience and Remote Sensing*, vol. 53, no. 1, pp. 207–218, Jan 2015.

[4] C. S. Ruf, C. T. Swift, A. B. Tanner, and D. M. L. Vine, "Interferometric synthetic aperture microwave radiometry for the remote sensing of the earth," *IEEE Trans. on Geosci. and Remote Sens.*, vol. 26, no. 5, pp. 597–611, Sep 1988.

[5] I. Corbella, N. Duffo, M. Vall-llossera, A. Camps, and F. Torres, "The visibility function in interferometric aperture synthesis radiometry," *IEEE Trans. Geosci. Remote Sens.*, vol. 42, no. 8, pp. 1677–1682, Aug 2004.

[6] A. Camps, "Application of interferometric radiometry to earth observation," Ph.D. dissertation, Polytechnic University of Catalonia, 11 1996.

[7] A. Camps, J. Bara, I. C. Sanahuja, and F. Torres, "The processing of hexagonally sampled signals with standard rectangular techniques: application to 2-d large aperture synthesis interferometric radiometers," *IEEE Trans. on Geosci. and Remote Sens.*, vol. 35, no. 1, pp. 183–190, Jan 1997.

[8] C. Zhang, H. Liu, J. Wu, S. Zhang, J. Yan, W. Sun, and H. Li, "Imaging performance analysis for the geostationary interferometric microwave sounder (gims) demonstrator," in *2012 12th Specialist Meeting on Microwave Radiometry and Remote Sensing of the Environment (MicroRad)*, March 2012, pp. 1–4.

[9] A. Sugihara El Maghraby, A. Grubisic, C. Colombo, and A. Tatnall, "A novel microwave radiometer concept using formation flight interferometry for geostationary atmospheric sounding," *IEEE Transactions on Geoscience and Remote Sensing*, vol. PP, no. 99, pp. 1–15, 2018.

[10] A. Averbuch, R. Coifman, D. Donoho, M. Elad, and M. Israeli, "Fast and accurate polar fourier transform," *Applied and Computational Harmonic Analysis*, vol. 21, no. 2, pp. 145 – 167, 2006. [Online]. Available: http://www.sciencedirect.com/science/article/pii/S1063520305001065

[11] N. Chou, J. A. Izatt, and S. Farsiu, "Generalized pseudo-polar fourier grids and applications in registering ophthalmic optical coherence tomography images," in *2009 Conference Record of the Forty-Third Asilomar Conference on Signals, Systems and Computers*, Nov 2009, pp. 807–811.

[12] D. H. Bailey and P. N. Swarztrauber, "The fractional fourier transform and applications," *SIAM Review*, vol. 33, no. 3, pp. 389–404, 1991. [Online]. Available: https://doi.org/10.1137/1033097

[13] W. G. Hawkins, "Fft interpolation for arbitrary factors: a comparison to cubic spline interpolation and linear interpolation," in *Nuclear Science Symposium and Medical Imaging Conference, 1994., 1994 IEEE Conference Record*, vol. 3, Oct 1994, pp. 1433–1437 vol.3.

[14] L. Shepp and B. Logan, "The fourier reconstruction of a head section," *IEEE Trans. on Nuclear Sci.*, vol. 21, no. 3, pp. 21–43, June 1974.

[15] A. Camps, H. Park, J. Bandeiras, J. Barbosa, A. Sousa, S. dAddio, and M. Martin-Neira, "Microwave imaging radiometers by aperture synthesisperformance simulator (part 1): Radiative transfer module," *Journal of Imaging*, vol. 2, no. 2, 2016.

[16] A. Camps, J. Bar, F. Torres, and I. Corbella, "Extension of the clean technique to the microwave imaging of continuous thermal sources by means of aperture synthesis radiometers," *Progress In Electromagnetics Research*, vol. 18, pp. 67–83, 1998.